

## Reproducible and Irreproducible Components in Ensemble Simulations with a Regional Climate Model

LEO SEPAROVIC,\* RAMON DE ELÍA,\*<sup>+</sup> AND RENÉ LAPRISE\*

*Canadian Network for Regional Climate Modelling and Diagnostics, Montréal, Quebec, Canada*

(Manuscript received 25 September 2007, in final form 7 February 2008)

### ABSTRACT

High-resolution limited-area models (LAMs) have been widely employed to downscale coarse-resolution climate simulations or objective analyses. The growing evidence that LAM climate statistics can be sensitive to initial conditions suggests that a deterministic verification of LAM solutions in terms of finescale atmospheric features might be misguided. In this study a 20-member ensemble of LAM integrations with perturbed initial conditions, driven by NCEP–NCAR reanalyses, is conducted for a summer season over a midlatitude domain. Ensemble simulations allow for the separation of the downscaled information in two parts: a unique, reproducible component associated with lateral-boundary and surface forcing, and an irreproducible component associated with internal variability. The partition in the reproducible and irreproducible components and their seasonal statistics is examined as a function of horizontal length scale, geographical position within the domain, height, and weather episodes during the season. The scale analysis of time-dependent model variables shows that, at scales smaller than a few hundred kilometers, the irreproducible component dominates, on average, the model solution, implying that the downscaled information at these scales is mainly in stochastic form. The constraint exerted by the surface forcing on the internal variability is weak. For seasonal averages, the reproducible component dominates at all scales, although for precipitation the reproducible and irreproducible components are of the same order of magnitude at scales smaller than 150 km. These results imply a need for a probabilistic approach to LAM climate simulations and their verification, especially for shorter integration times, from months to seasons.

### 1. Introduction

Study of the climate system through the use of high-resolution atmospheric general circulation models (GCMs) coupled with land surface, ocean, and sea ice represents a tremendous computational cost, which is out of reach for many research centers. Regional climate models (RCMs) are frequently employed to provide lower-cost climate simulations using high-resolution representations of the atmospheric dynamics and

physics, as well as forcing at the interface between the atmosphere and the other components of the climate system, over only a specified area of the globe [see Giorgi and Mearns (1999) for a review]. The most popular approach in regional climate modeling so far has been the “one way” nesting strategy. This method involves the relaxation of high-resolution limited-area model (LAM) variables in the vicinity of the domain lateral boundaries to the externally prescribed coarse-resolution fields derived from GCM simulations or objective analyses (Davies and Turner 1977).

From a downscaling perspective, the one-way nesting strategy should allow for generation of finescale spatiotemporal weather structures with appropriate amplitudes. This is necessary if high-resolution nested LAMs are to be able to realistically simulate important mesoscale atmospheric features such as fronts and precipitations lines (Denis et al. 2002b). To date, the assessment of value added by LAM integrations has been a rather difficult task, as the observations are too sparse

---

\* Additional affiliation: Université du Québec à Montréal, Montréal, Quebec, Canada.

+ Additional affiliation: Ouranos Consortium, Montréal, Quebec, Canada.

---

*Corresponding author address:* Leo Separovic, UQAM, Ouranos, 550 Sherbrooke St. West, 19th Floor, West Tower, Montréal, QC H3A 1B9, Canada.  
E-mail: separovi@sca.uqam.ca

for construction of distributions of atmospheric variables without significant uncertainty at scales from hundreds to tens of kilometers over many areas of the globe. In response, indirect techniques based on virtual reality datasets have been developed in order to examine possible conceptual limitations of the one-way nesting with respect to the ability of LAMs to generate correct amplitudes and statistics of finescale structures; these studies support an optimistic point of view regarding the issue of the generation of finescales in LAMs [see Laprise et al. (2008) for a review].

There has been growing evidence that LAMs can display chaotic behavior, although different from that in GCMs. The differences among global model integrations from slightly perturbed initial conditions (IC) increase until they become saturated at a value approximately equal to the climatological transient-eddy variability implying that the members of the ensemble become on average uncorrelated (e.g., Lorenz 1969, 1982; Schubert and Suarez 1989). Analogous experiments with one-way nested LAMs show that the inter-member variance asymptotes to notably smaller values than the transient-eddy variance (Anthes et al. 1985). This has been attributed to the forcing exercised by the lateral boundary conditions (LBCs; Vukicevic and Paegle 1989; Vukicevic and Errico 1990) or topography and surface heterogeneities (van Tuyl and Errico 1989). The intrinsic level of internal variability in LAMs appears to be independent of the agent (LBC or IC) and the magnitude of the imposed perturbations (Giorgi and Bi 2000; Caya and Biner 2004).

A scale analysis of the growth of the forecast error in LAMs in studies by Laprise et al. (2000) and de Elía et al. (2002) showed that the magnitude of the error is scale sensitive, the finest scales being the most affected. This led the authors to conclude that nested LAMs, despite generating significant finescale weather features, might be futile if they are used to provide the right time and position of finescale weather patterns. Internal variability can be also a nuisance in studies of the sensitivity of an RCM's climate to parameter changes (Weisse et al. 2000). Furthermore, in several studies the magnitude of the internal variability of seasonal averages of hydrologically relevant variables was found locally to be comparable to that in global models (Jones et al. 1997; Christensen et al. 2001; Rinke et al. 2004; Alexandru et al. 2007). However, Denis et al. (2002b) found lower-moment seasonal statistics of fine-scale atmospheric fields derived from nested LAM integrations to be rather skillful, especially for low-level variables. Giorgi and Bi (2000) and Caya and Biner (2004) also reported that perturbations in the ICs had

little effect on lower-moment statistics of climate variables in their LAM simulations.

Alexandru et al. (2007) performed a systematic study of internal variability with a 20-member ensemble of one-summer-season LAM integrations with perturbed ICs, conducted over several domains of different sizes, covering the east coast of North America. The authors found that internal variability displays preferential regions within the domain, depending on the variable. Changes in domain size altered considerably the geographical distribution and magnitude of the internal variability, both for time-dependent variables and their seasonal averages. However, a common feature of ensembles conducted over different domains was the fact that the maximum scatter among members in 6-hourly mean precipitation occurred in the southeastern United States and was associated with convection in the moist air advected from the Gulf of Mexico over the warm continental surface; the spread in seasonal average precipitation was locally comparable to that in GCMs. The maximum spread in instantaneous geopotential height was found downstream of the area of the maximum scatter in precipitation. The authors suggested that the intense convection triggered small-scale perturbations in the mass field that grew in magnitude and increased in length scale while being advected by the general circulation. It has been shown that the fast growth and upscale propagation of initial errors in the early stages of LAM simulations are likely associated with conditional instability and moist convection; this is documented in several studies of LAM predictability and error growth (e.g., Zhang et al. 2003, 2007; Tan et al. 2004).

The aforementioned findings imply that a part of the downscaled weather features in nested LAMs is in the form of an externally forced signal, independent of perturbations in the IC and in this sense reproducible. On the other hand, the presence of internal variability—that is differences between members driven by the same lateral and surface boundary conditions—implies the existence of an irreproducible component of stochastic nature. The purpose of this study is to identify and examine the relative significance of these two components in dynamical downscaling by LAMs, in terms of the model variables, horizontal length scale, geographical position within the domain, height and weather episodes within a summer season. To this end, a quantity called reproducibility is defined and analyzed as a measure of the relative significance of the reproducible component within the RCM solution. It is worth stressing that herein the reproducibility should be interpreted as the degree to which the model's response is exclusively dependent on boundary forcing,

rather than as an ability of the model to reproduce the real atmosphere as a reference; the reproducibility in the latter sense is not studied here.

This work is organized as follows. In section 2 the experimental setup is presented. In section 3 we examine the spectral behavior of the reproducibility, which provides evidence of how the downscaled information is partitioned between the self-reproducible signal and the internal variability at different length scales. The geographical distribution of the reproducibility is presented in section 4. In section 5 we examine the reproducibility of the seasonal averages. The findings are summarized and discussed in section 6.

## 2. Experimental setup

The RCM used in this study is version 3.6.1 of the Canadian Regional Climate Model (CRCM) described in Caya and Laprise (1999). The CRCM is a limited-area gridpoint model based on fully elastic nonhydrostatic Euler equations discretized in time by a three-time-level semi-Lagrangian semi-implicit scheme. The physical parameterizations are similar to those described in Caya and Laprise (1999) with the exception of the moist convection scheme, which follows the formulation of Bechtold et al. (2001).

In the horizontal, the computations are performed on a staggered Arakawa C grid in polar-stereographic coordinates, with a nominal gridpoint spacing of 45 km, true at 60°N. In the vertical, 18 model levels, defined by a geometric terrain-following Gal-Chen scaled height, were used (Gal-Chen and Somerville 1975). The time step used in this experiment was 15 min. The nesting technique, developed by Robert and Yakimiw (1986) and Yakimiw and Robert (1990), as proposed by Davies (1976), is based on the relaxation of the horizontal velocity components of the CRCM toward the driving fields in a nine-point-wide zone along the lateral boundaries. A complete description of the nesting technique including the dynamical formulation of the CRCM can be found in Laprise et al. (1997).

At the lateral boundaries the CRCM requires information of horizontal velocity, temperature, surface pressure, and specific humidity at each time step. The same set of variables is necessary to define the initial state. In the present study, both the LBCs and the ICs are derived from the National Centers for Environmental Prediction–National Center for Atmospheric Research (NCEP–NCAR) reanalyses (Kalnay et al. 1996). The LBCs are provided linearly by interpolating the 6-hourly NCEP–NCAR reanalyses on the CRCM grid at each time step.

The set of prognostic variables in the CRCM includes

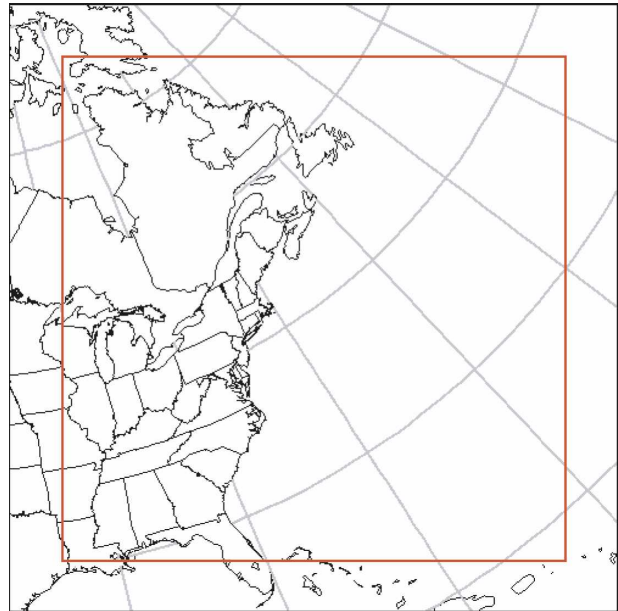


FIG. 1. The integration domain of the CRCM. The ribbon beyond the red line denotes the relaxation zone that is excluded from the analysis.

surface variables such as surface temperature, liquid and frozen soil water fraction, and amount and age of snow. These fields are initialized by their climatological values, while the ocean surface variables are prescribed from Atmospheric Model Intercomparison Project (AMIP) data (Gates 1992).

An ensemble of 20 CRCM simulations was generated from May to the end of August 1993 over a domain of  $121 \times 121$  grid points covering eastern North America and the western North Atlantic Ocean (Fig. 1). All the simulations were driven by the same LBCs and ocean surface data. The simulations of the members in the ensemble were launched 24 h apart, starting at 0000 UTC 1 May 1993; thus, the last member of the ensemble started at 0000 UTC 20 May 1993. The 3-month period of June–August 1993 is studied. The spinup period hence varies from 11 to 30 days. A detailed description of this ensemble may be found in Alexandru et al. (2007). The domain of analysis consists of  $101 \times 101$  grid points, exclusive of the nine-point relaxation zone, covering the internal domain area shown in Fig. 1.

## 3. Analysis of reproducible and irreproducible components of simulated spatial variance

### a. Definition of the reproducible and irreproducible components of model variables

Let us denote with  $X = X_{ijkmn}$  the  $n$ th realization of a variable  $X$  within an ensemble of  $N$  simulations ( $N =$

20 here), defined on a rectangular horizontal grid ( $i, j$ ) with  $I \times J$  computational points ( $I = J = 101$  here) at a pressure level indexed by  $k$ , and sampled at times  $t_0 + m\Delta t$ ,  $m = \{1, 2, \dots, M\}$  (here  $M = 369$  because fields are sampled every  $\Delta t = 6$  h during the three summer months and  $t_0$  is 0000 UTC 1 June 1993).

The externally forced, reproducible part of the variable  $X$  is obtained by the ensemble average defined as

$$\langle X \rangle_{ijkm} \equiv \frac{1}{N} \sum_{n=1}^N X_{ijkmn}. \quad (1)$$

Deviations from the ensemble average, defined as

$$X_{ijkmn}^* \equiv X_{ijkmn} - \langle X \rangle_{ijkm}, \quad (2)$$

sample what is referred to as the irreproducible part of the variable  $X$ . The statistics of the ensemble deviations can be summarized by the standard deviation:

$$\varepsilon_{ijkm} \equiv \langle (X_{ijkmn}^*)^2 \rangle^{1/2}. \quad (3)$$

To illustrate the reproducible and irreproducible components using these definitions, we present in Fig. 2 an example of their application. Figure 2a shows specific realizations of geopotential height at 925 hPa at 0000 UTC 25 July 1993. The black, red, and blue lines represent three realizations selected from the 20-member ensemble. The ensemble mean computed from all 20 of the members of the ensemble is shown in Fig. 2b; this reproducible component of the mass field is devoid of finescale details that characterized each of the three realizations shown in Fig. 2a, which indicates the nonreproducible nature of these features. Figure 2c shows the standard deviation of the members of the ensemble. Finally, NCEP–NCAR reanalyses utilized to drive the model are presented in Fig. 2d. For the situation analyzed here, very little of the finescale features present in the individual CRCM realizations has survived the ensemble averaging. It is also worth noting that considerable differences are present between the ensemble average and the NCEP–NCAR reanalyses.

We now turn our attention to relative vorticity, a field much more dominated by the small-scale components than geopotential height. The relative vorticity at 925 hPa is shown in Fig. 3 for the three selected realizations of the geopotential height shown in Fig. 2a. In the case of vorticity, the ensemble average retains an important amount of small-scale details. For example, the filament of positive vorticity south of Labrador associated with a cold front is well preserved, as well as the maximum over the southeastern United States. This is much less the case over the Atlantic, where a lot of the weather features are lost in the ensemble average. Unlike the case for geopotential height, the CRCM en-

semble average vorticity (Fig. 3b) does add information on finescales to the NCEP–NCAR driving fields (Fig. 3d). This implies that, for instantaneous relative vorticity, a considerable part of the finescale details is generated in reproducible form. For example, the local maximum of vorticity over the Great Lakes associated with a warm front (see also Fig. 2a) appears to be almost completely reproducible, as its intensity is not much reduced in the ensemble mean and the standard deviation of the ensemble is small there (Fig. 3c). Comparison of the standard deviation computed for geopotential height (Fig. 2c) and vorticity (Fig. 3c) shows that, locally, ensemble spread in one simulated variable does not necessarily imply the spread in other variables, as there is significant spread in geopotential height but little spread in vorticity associated with the warm front over the Great Lakes.

Figure 4 illustrates the decomposition of the geopotential height at 925 hPa at another time: 0000 UTC 20 June 1993. From Fig. 4a it can be inferred that there are few noticeable large-scale differences among the members of the ensemble (now all 20 realizations are shown). Some small-scale differences are nevertheless still present. The most notable small-scale differences occur over the continental area. It is worth noting that the Midwest low pressure system combined with a strong ridge over the southeastern United States are responsible for the advection of moist air over the large part of the continental area of the domain. The moist convection associated with such a situation might have triggered these small-scale differences, as suggested in Zhang et al. (2003). Another important area of small-scale differences is situated along the frontal zone associated with the trough from the Labrador low pressure. These features are not noticeable in the reproducible part, that is, the ensemble mean (Fig. 4b), but can be found as weak maxima of the standard deviation of the ensemble shown in Fig. 4c, indicating their predominantly irreproducible nature. Comparison of CRCM-simulated and NCEP–NCAR-analyzed fields (Fig. 4d) shows considerable systematic discrepancies, as the large-scale low pressure system observed over the Atlantic is absent from all the realizations of the CRCM ensemble.

The corresponding relative vorticity is shown in Fig. 5. Comparison of the simulated vorticity (Fig. 5a) with NCEP–NCAR reanalyses (Fig. 5d) shows that the model does add the finescale spatial details to the coarse-resolution driving fields. Further, as there is little spread among the CRCM members, most finescale features are well preserved in the ensemble average (Fig. 5b), which implies that at this time the CRCM

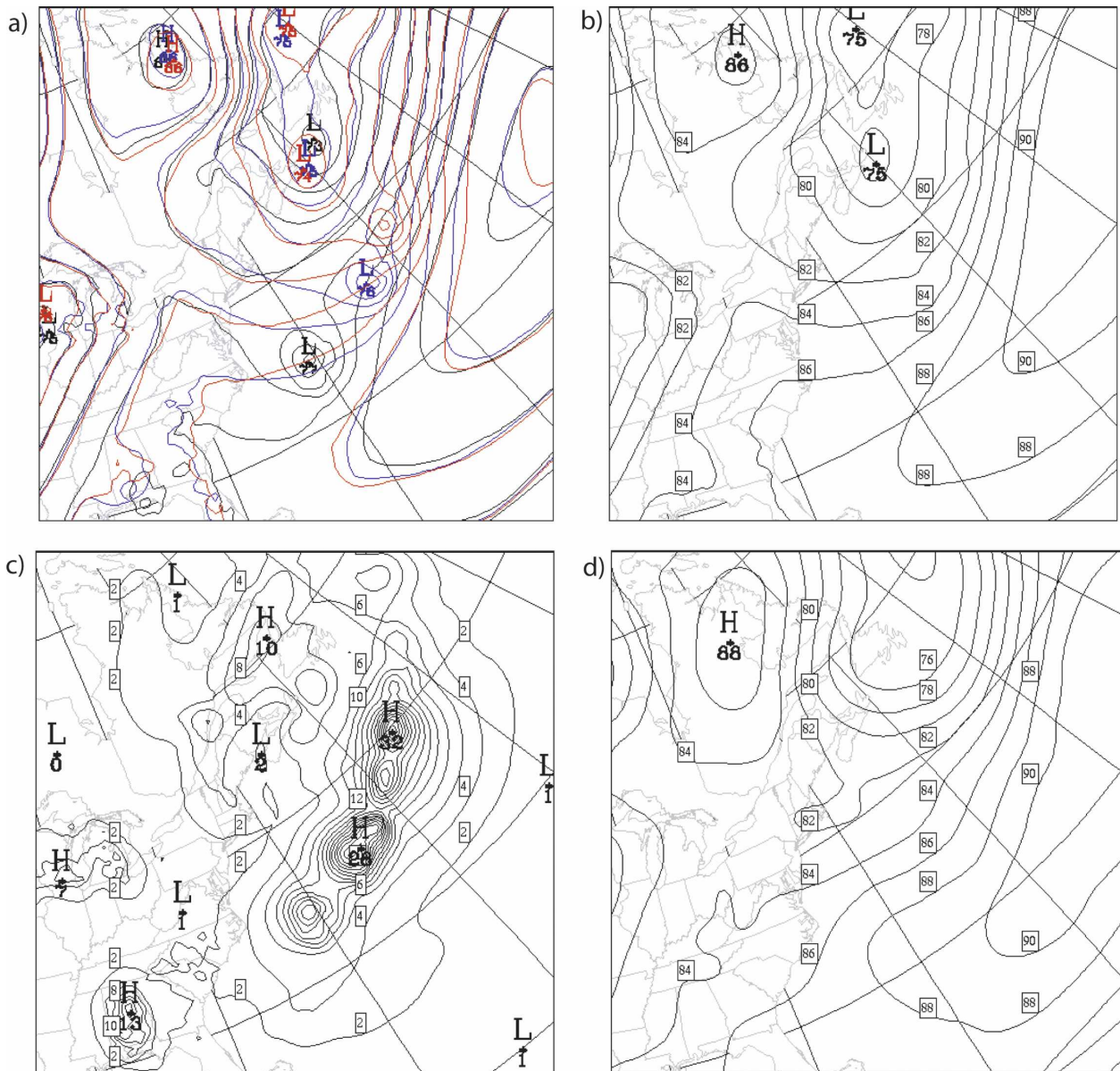


FIG. 2. Geopotential height at 925 hPa at 0000 UTC 25 Jul 1993: (a) three selected realizations (dam), (b) the ensemble mean of the 20 realizations (dam), (c) the standard deviation of the ensemble (m), and (d) NCEP-NCAR reanalyses projected on the CRCM grid (dam).

generates finescale vorticity features in reproducible form.

*b. Power spectra of reproducible and irreproducible components*

To reveal what spatial scales are more or less reproducible, we have applied a spectral analysis to the ensemble of the simulations. The separation of scales is performed utilizing two-dimensional discrete cosine transform (DCT), introduced into the analysis of me-

teological fields by Denis et al. (2002a). The two-dimensional power spectrum of a field  $X$ , computed at a selected pressure level, can be expressed as a scalar function,  $S_q(X_{ijkmn})$ , of nondimensional scalar wavenumber  $q$ , such that  $q \in \{1, 2, \dots, (I - 1)/2\}$ , where  $I$  denotes the number of computational points along one side of the domain of analysis ( $I = 101$  here),  $(i, j)$  are the grid indices, and  $k, m$ , and  $n$  denote the level index, the sampling time, and the realization of the ensemble, respectively. The length scale corresponding to wavenumber  $q$  can be computed as

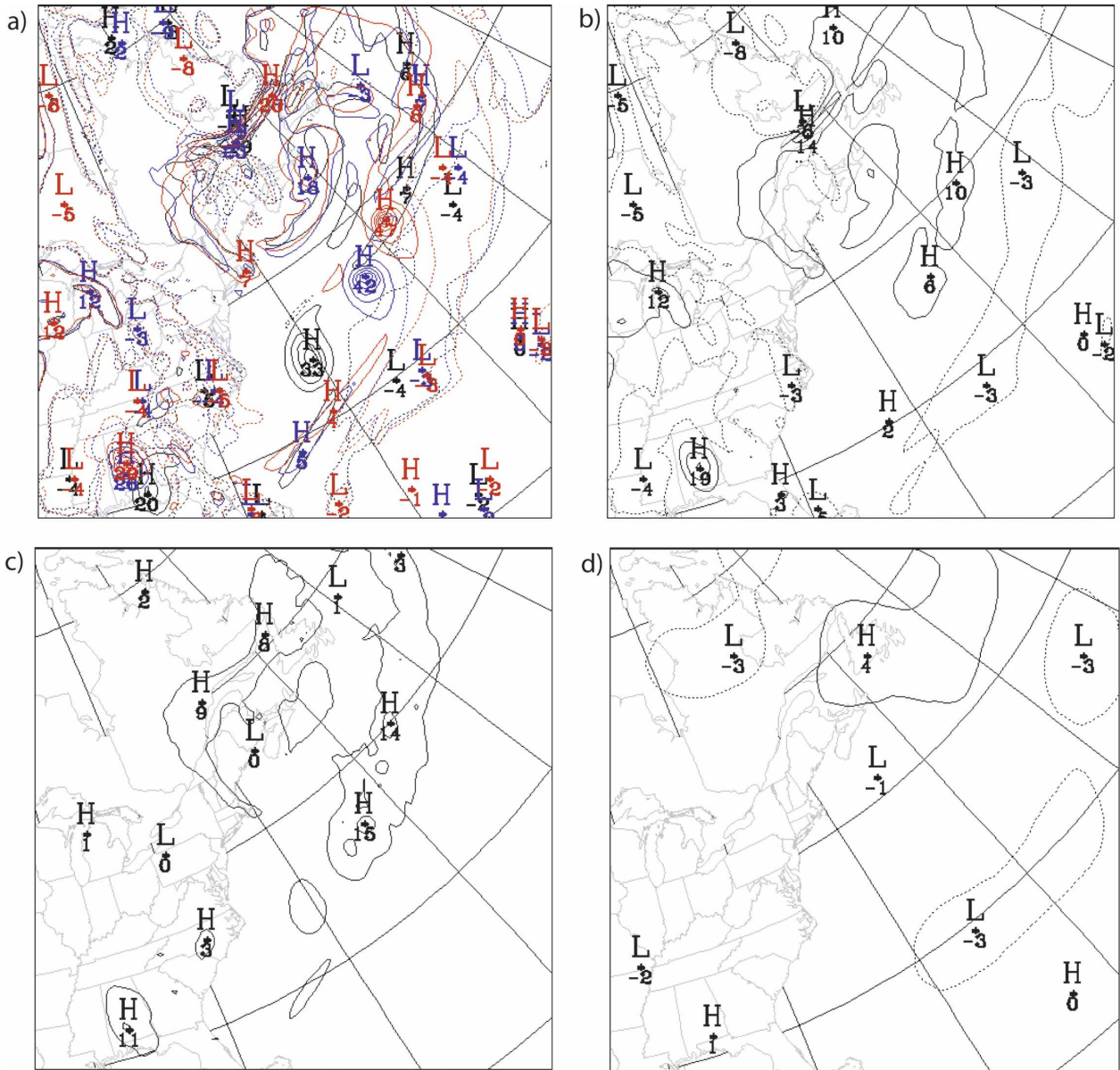


FIG. 3. Relative vorticity at 925 hPa at 0000 UTC 25 Jul 1993 ( $\times 10^{-5} \text{ s}^{-1}$ ): (a) three selected realizations, (b) the ensemble average of the 20 realizations, (c) the standard deviation of the ensemble, and (d) regrided NCEP-NCAR reanalyses. Solid lines are used for positive values, and dotted lines are used for negative values of relative vorticity.

$$l_q = \frac{(I - 1)\Delta}{q}, \quad (4)$$

where  $\Delta$  is the grid spacing, 45 km here. Therefore, the largest resolved length scale is 4500 km, while the Nyquist wavelength is 90 km. It is also worth noting that, when summed over all defined wavenumbers  $q$ , the power spectrum of a given field computed at a given pressure level is equal to its domain-average variance at that level.

Three additional power spectra can be defined:

$$S_{qkm}^A \equiv \langle S_q(X_{ijkmn}) \rangle, \quad (5)$$

$$S_{qkm}^R \equiv S_q(\langle X \rangle_{ijkm}), \quad \text{and} \quad (6)$$

$$S_{qkm}^I \equiv \langle S_q(X_{ijkmn}^*) \rangle. \quad (7)$$

Here,  $S^A$  represents the ensemble average of the power spectra of the  $N = 20$  members of field  $X$  in CRCM simulations. It can be interpreted as the average power generated by individual realizations. The quantity  $S^R$  is the power spectrum of the ensemble average. The

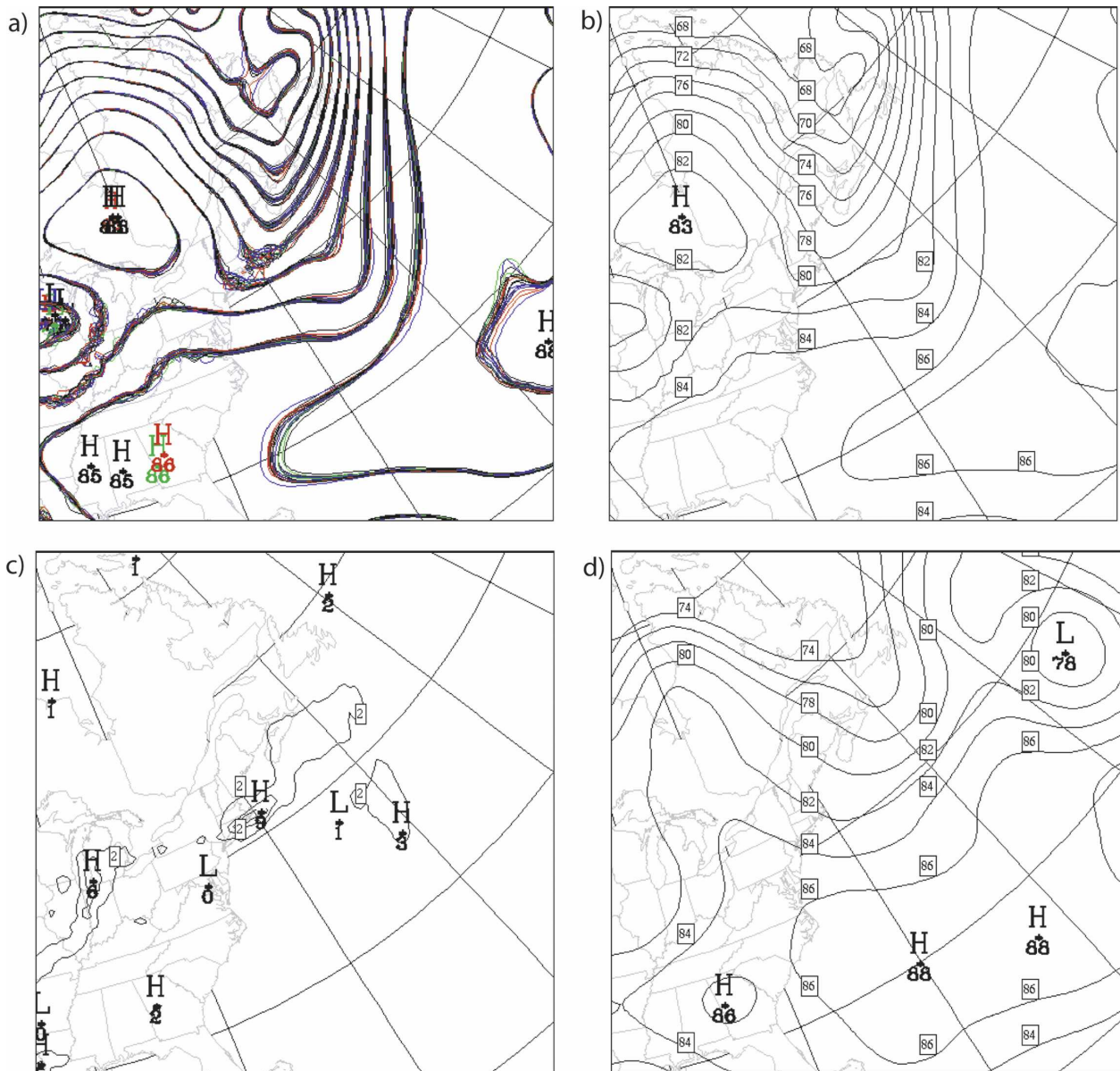


FIG. 4. As in Fig. 2 but for geopotential height at 925 hPa at 0000 UTC 20 Jun 1993.

quantity  $S^I$  is the ensemble average of the power spectra of the individual members' deviations from the ensemble average. It is shown in the appendix that the three spectra satisfy the following relation:

$$S_{qkm}^A = S_{qkm}^R + S_{qkm}^I. \quad (8)$$

Hence, the average power spectrum  $S^A$  is decomposed into the power of the reproducible component ( $S^R$ ) associated with the external forcing and identifiable with the ensemble average, and the average power of the irreproducible component ( $S^I$ ) sampled by deviations

about the ensemble average. This approach is analogous to that used by Boer (2003).

The three power spectra computed for the ensemble of realizations of geopotential height at 0000 UTC 25 July 1993 (shown in physical space in Fig. 2) are shown in Fig. 6a. This corresponds to the situation characterized by a large spread between members. The spectra  $S^A$ ,  $S^R$ , and  $S^I$  are represented by solid, dashed, and dotted lines, respectively. It can be seen that the large scales are dominated by the reproducible component  $S^R$ . The relative contribution of the irreproducible component  $S^I$  increases from length scales of 1500–500 km

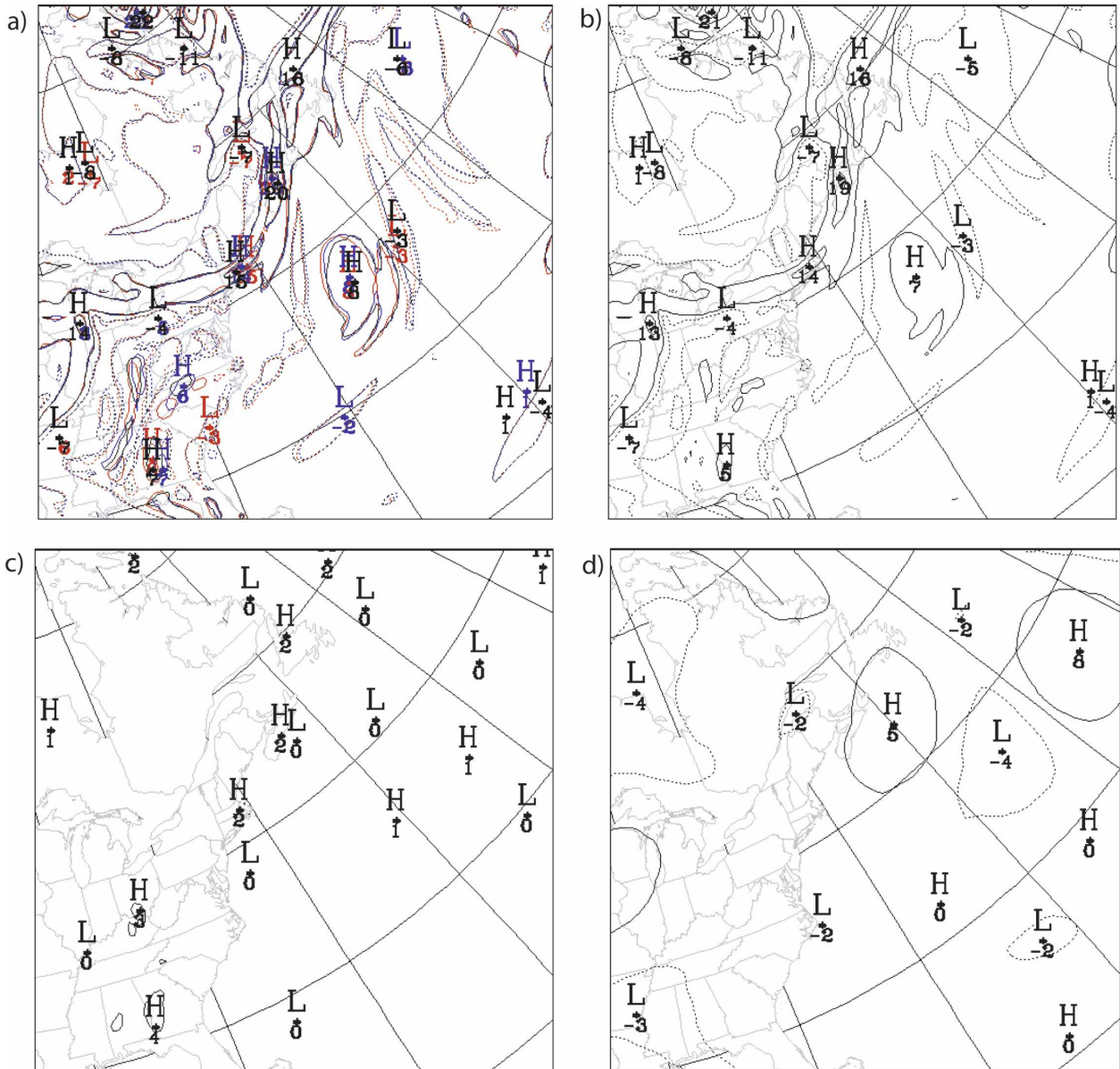


FIG. 5. As in Fig. 3 but for relative vorticity at 925 hPa at 0000 UTC 20 Jun 1993.

and this component dominates at length scales smaller than 500 km. Also shown in Fig. 6a is the power spectrum of the driving fields (NCEP–NCAR reanalyses) interpolated onto the CRCM grid (the red line); this quantity is denoted by  $S^D$ . The steplike decrease in its power at around 1000 km indicates the effective resolution of NCEP–NCAR reanalyses used to initialize and nest the CRCM simulations. The power does not drop to zero, as might be expected, because the interpolation on the CRCM grid and aliasing in the DCT contaminate the spectrum with some noise. However, that noise has less power than the reproducible com-

ponent of the CRCM simulations. This means that the ensemble average does generate spatial variance at small scales.

Figures 6b–d show the decomposed power spectra of the relative vorticity (discussed earlier in relation to Fig. 3), divergence, and 6-hourly precipitation at the same instant. The relative vorticity and divergence have much more variance at intermediate and small-scale ranges; that is, their spectra are much less steep. Thus, at small scales, the difference between simulated power and that of regridding noise present in the NCEP–NCAR curve shows the CRCM has the ability to add

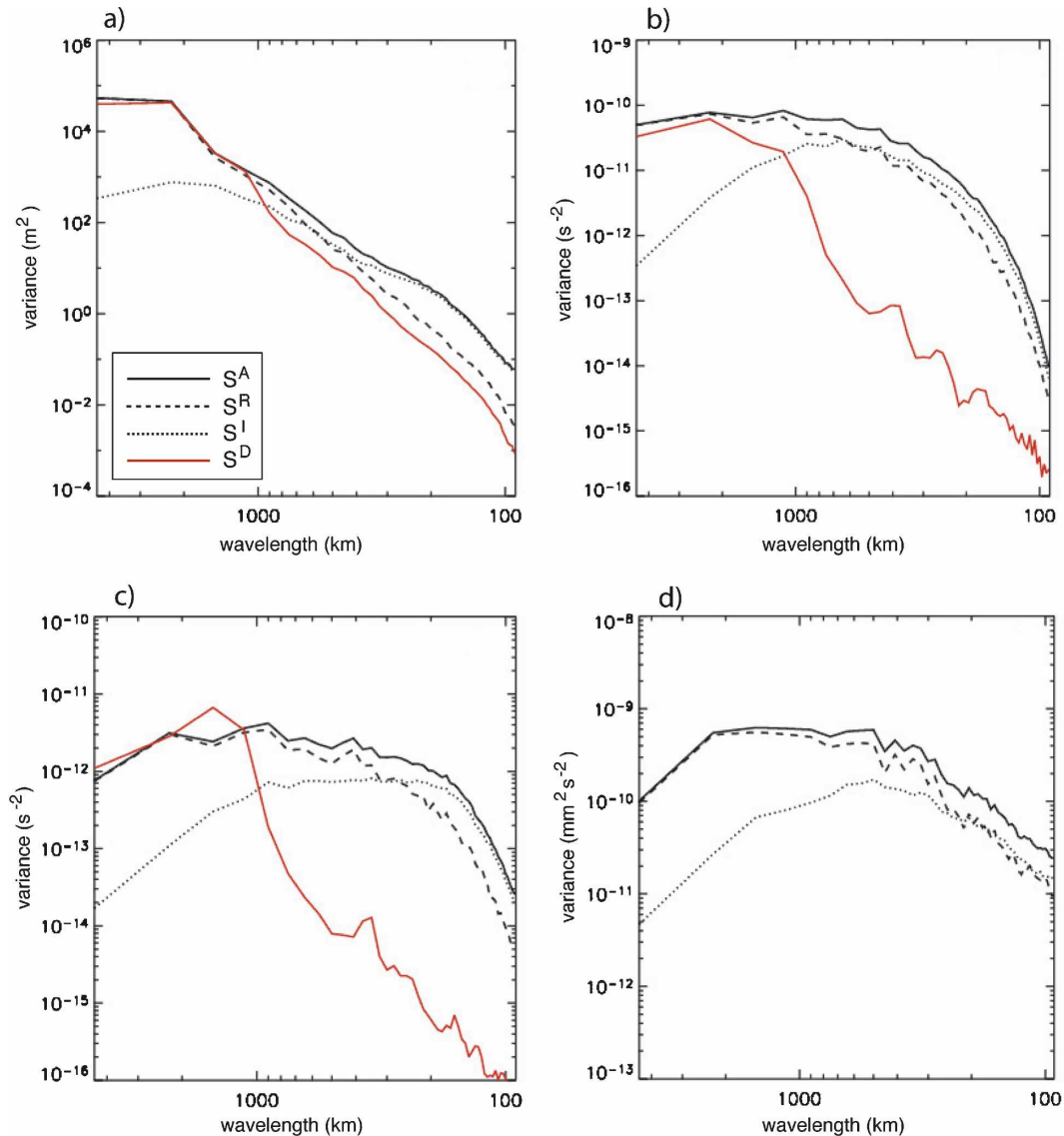


FIG. 6. Decomposition of power spectra at 0000 UTC 25 Jul 1993 for (a) geopotential height, (b) vorticity, (c) divergence, all at 925 hPa, and (d) 6-hourly precipitation. Solid line represents the ensemble average of the members' power spectra,  $S^A$ , defined in Eq. (5); the dashed line represents its reproducible part  $S^R$  [Eq. (6)]; and the dotted line is its irreproducible part  $S^I$  [Eq. (7)]. The red line is the spectral variance of the regridded NCEP-NCAR reanalyses (not available for precipitation).

variance at scales finer than the resolution of the driving data, which is necessary (but not sufficient) for the model to add value.

When relative vorticity is considered (Fig. 6b), the CRCM spectral power in the irreproducible component starts to be of the same order of magnitude as the power of the reproducible component at length scales of 1200 km. At 650 km the irreproducible and reproducible components are equal and at finer scales, the irreproducible component dominates the power spectrum. The power spectrum of the divergence (Fig. 6c)

reveals that the internal variability is confined to length scales smaller than 300 km. For 6-hourly mean precipitation (Fig. 6d), the crossover occurs at even shorter length scales of around 200 km.

Figure 7 shows a similar decomposition of the power spectrum for the situation at 0000 UTC 20 June 1993, which is characterized by low ensemble spread and which was examined earlier in Figs. 4 and 5. The crossover of the reproducible and irreproducible components for geopotential height (Fig. 7a) now lies at length scales of approximately 300 km. Relative vorticity (Fig.

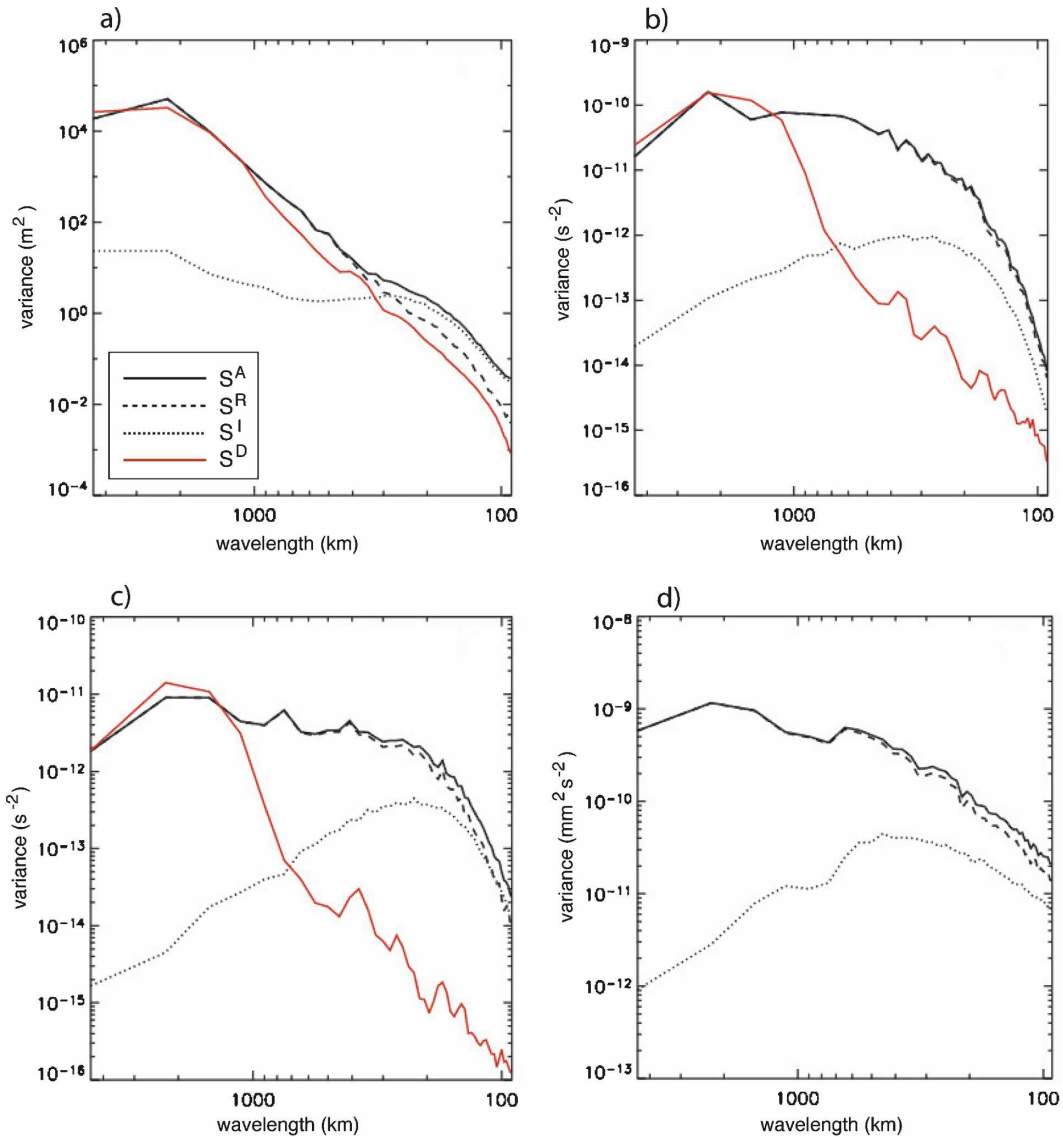


FIG. 7. As in Fig. 6 but at 0000 UTC 20 Jun 1993.

7b) exhibits very distinct spectral behavior with almost its entire power spectrum contained in the reproducible component. For divergence (Fig. 7c) and precipitation (Fig. 7d), the irreproducible component reaches the order of magnitude of the reproducible at scales smaller than roughly 300 km.

The two examples examined in this section illustrate that the relative contributions of the reproducible and irreproducible (internal variability) components of the model solution can vary substantially during the integration period depending on the weather pattern. In the following, we examine the time evolution of these components through one summer season.

*c. Reproducibility ratio*

For the purposes of evaluating the relative level of reproducibility as a function of spatial scales and time, we define a reproducibility ratio as follows:

$$\rho_{qkm} \equiv \frac{S_{qkm}^R}{S_{qkm}^A}, \tag{9}$$

where  $q$  is the wavenumber,  $k$  is the level index, and  $m$  denotes the sampling time. This ratio takes values between 0 and 1; it approaches 1 when the members of the ensemble are very similar, that is, the simulations are dominated by the reproducible component and internal

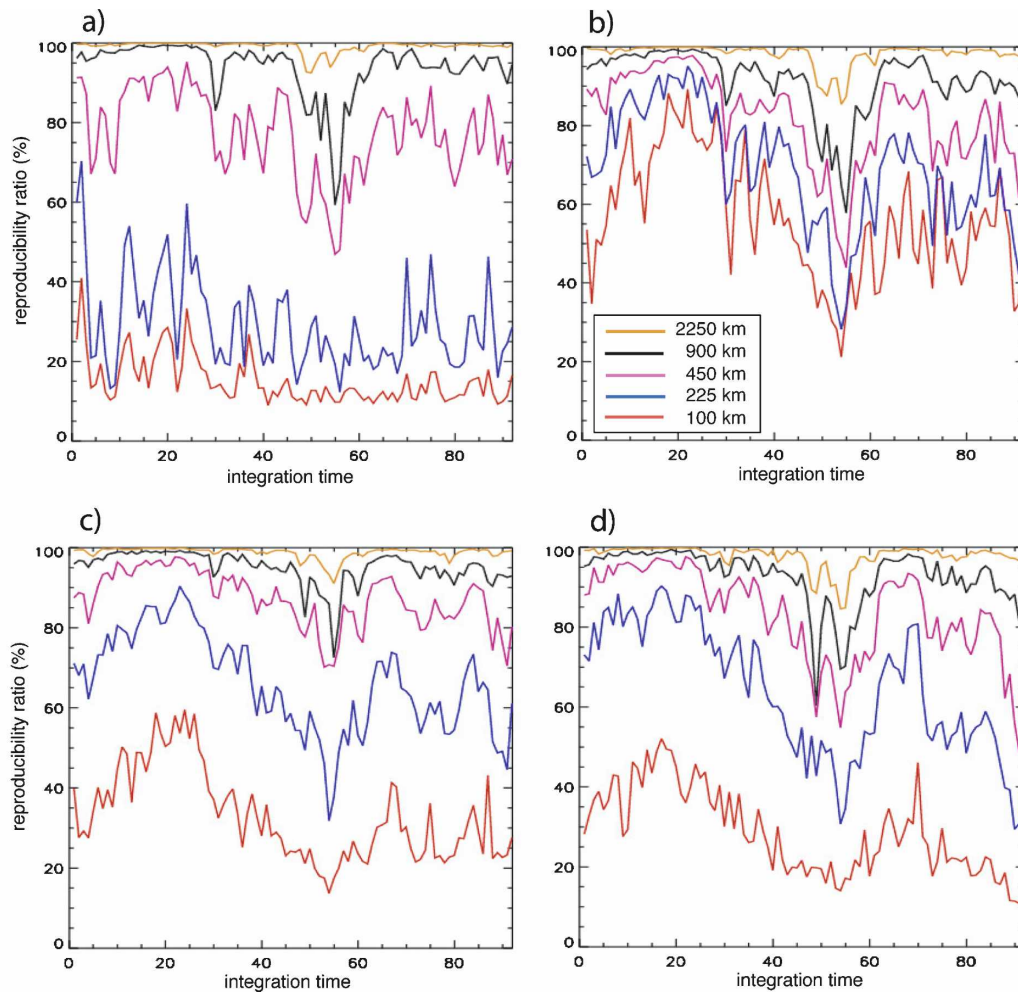


FIG. 8. Reproducibility ratio as a function of time at different length scales for (a) geopotential height, (b) vorticity, and (c) divergence, all at 925 hPa, and (d) 6-hourly precipitation: yellow, 2250 km; black, 900 km; purple, 450 km; blue, 225 km; and red, 100 km.

variability is weak, and approaches 0 when the irreproducible component dominates.

Time series of the reproducibility ratio for geopotential height, vorticity, and divergence at 925 hPa, as well as 6-hourly precipitation, are shown in Fig. 8 (in percentages). Five length scales are selected: 2250, 900, 450, 225, and 100 km. To make the graphs more readable, the daily average of the reproducibility ratio is shown. Large time variations of the reproducibility ratio are present, and they occur in all variables displayed in Fig. 8. In general, the reproducibility ratio increases with length scales, but the variations of the reproducibility ratios with length scale differ greatly between variables. There is a sharp drop in geopotential height around 450 km (Fig. 8a) while it is gradual for other variables. Vorticity is the variable that exhibits the largest reproducibility at the shortest length scale compared to the other variables.

The small-scale divergence reproducibility ratio (Fig. 8c) is quite a bit smaller than that of the vorticity (Fig. 8b). The precipitation reproducibility ratio (Fig. 8d) closely follows that of the divergence. For example, at 100 km, it is most often below 40%; this may be a fingerprint of convection that dominates small-scale precipitation in summer and is associated with the divergent component of the flow.

The time-averaged power spectra  $\overline{S^A}$ ,  $\overline{S^R}$ , and  $\overline{S^I}$ , of the CRCM geopotential height, vorticity, and divergence at 925 hPa and precipitation are computed in Fig. 9; also shown are the time-averaged power spectra of the regrided NCEP–NCAR reanalysis,  $\overline{S^D}$ . For geopotential height (Fig. 9a), the reproducible component of the power spectrum dominates for scales larger than approximately 300 km while the irreproducible component dominates at smaller scales. For low-level divergence (Fig. 9c) and precipitation (Fig. 9d), the cross-

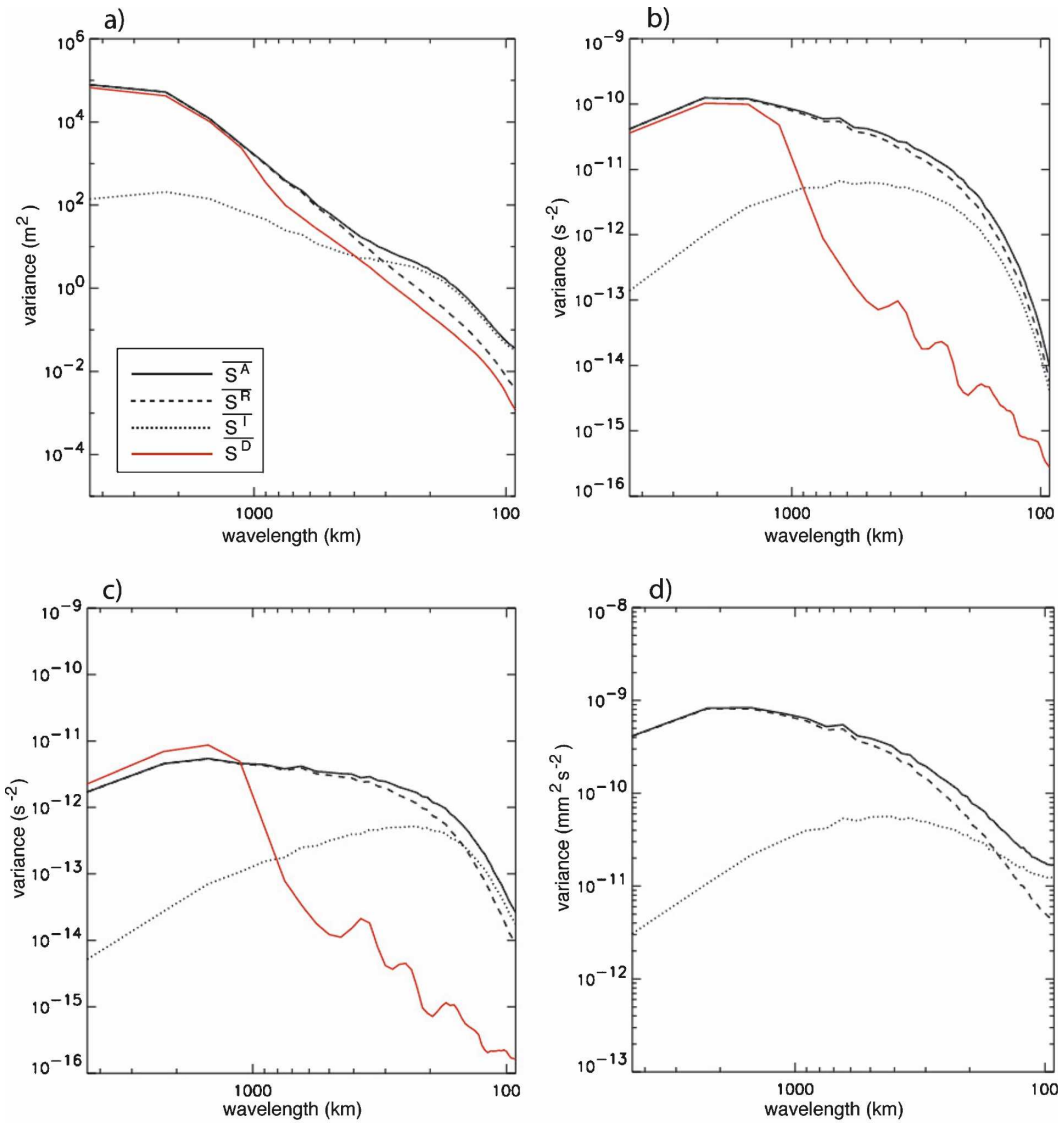


FIG. 9. Time-average power spectra of (a) geopotential height, (b) vorticity, (c) divergence, all at 925 hPa, and (d) 6-hourly precipitation: solid line,  $\overline{S^A}$ ; dashed line,  $\overline{S^R}$ ; dotted line,  $\overline{S^I}$ ; and red line, the power spectrum of the NCEP–NCAR reanalyses projected onto the CRCM grid.

over occurs at length scale of 150 km. Vorticity (Fig. 9b) on the other hand is on average dominated by the reproducible component at all length scales. It is worth noting that the power spectra of the NCEP–NCAR reanalyses and those of the CRCM simulations are not identical at large scales, indicating that the amplitude of the large-scale variables deviates systematically from that of the driving fields; we will study this in detail in the next subsection.

It is interesting that a small-scale-dominated variable, such as vorticity, is reproducible relatively well even at scales of 100 km. As shown earlier in Fig. 8b, the reproducibility ratio of small-scale vorticity compo-

nents exhibits the largest time variations among the variables. It is also tightly linked with the reproducibility ratio of its large-scale components: it appears that small-scale vorticity features are generally devoid of large differences among the members of the ensemble, unless the differences affect the large-scale components of the model variables. This is much less frequently the case with small-scale divergence (Fig. 8c), which permanently exhibits lower values and smaller time variations of reproducibility.

The vertical distribution of the reproducibility ratio of time-dependent CRCM variables is assessed by the following coefficient:

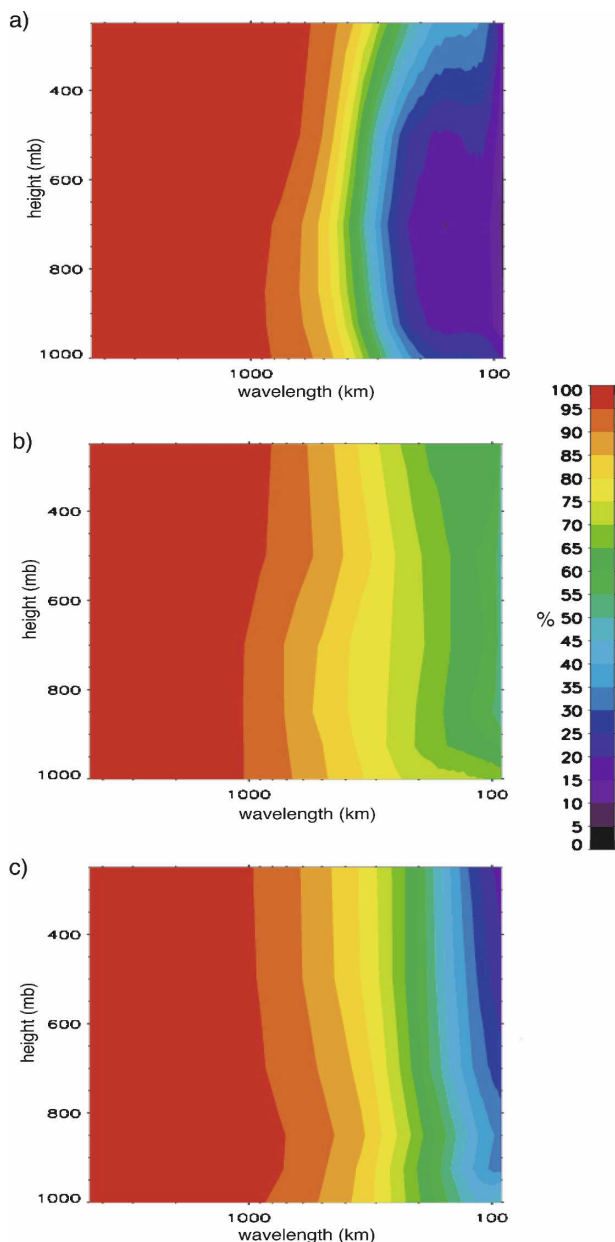


FIG. 10. Average reproducibility ratio [Eq. (10)] of the instantaneous CRCM variables (%) as a function of length scale and height: (a) geopotential height, (b) vorticity, and (c) divergence.

$$\rho_{qk} \equiv \frac{\overline{S_{qkm}^R}}{\overline{S_{qkm}^A}}. \quad (10)$$

Here, the overbar denotes the time average of the power spectra. Figure 10 shows the distribution of  $\rho_{qk}$  as a function of height and horizontal length scale, for geopotential height, vorticity, and divergence. At small scales, the values of  $\rho_{qk}$  are noticeably larger for vorticity than for the other variables (Fig. 10b); at scales

smaller than 200 km, geopotential height (Fig. 10a) and divergence (Fig. 10c) exhibit very small  $\rho_{qk}$ . However, in the region between 1000 and 600 hPa and 1000 and 500 km, the reproducibility ratio of the vorticity is somewhat smaller than those of other variables.

The vertical distribution shows that, at large and intermediate scales, the reproducibility of surface variables is not, on average, considerably higher than that aloft as might be expected if surface forcing exerted an important constraint to the internal variability at these scales. However, at scales smaller than 200 km, the reproducibility is increased near the surface; this is especially noticeable in cases of divergence (Fig. 10c). It is noteworthy that the domain of this study is characterized with modest topography and that ocean covers a large part of the domain.

#### d. Deviation of amplitudes of CRCM simulation with respect to NCEP–NCAR reanalyses

The ability of the model to reproduce the large-scale spatial variance of the driving fields is examined utilizing the following variance-excess coefficient [similar to that in Castro et al. (2005)]:

$$\eta_{qk} \equiv 1 - \frac{\overline{S_{qkm}^D}}{\overline{S_{qkm}^A}}. \quad (11)$$

Here,  $S^D$  denotes the power spectrum of driving the NCEP–NCAR reanalyses and  $S^A$  the ensemble average of the members' power spectra as given by Eq. (5). The overbar denotes the time average. The coefficient  $\eta_{qk}$  is equal to 0 when the average power of the CRCM fields and the power of the NCEP–NCAR reanalyses are identical. Further,  $\eta_{qk}$  takes positive (negative) values when the average members' power is larger (smaller) than that of the NCEP–NCAR fields. Particularly, at small scales that are not resolved by the driving fields, the optimal value of the coefficient  $\eta_{qk}$  is 1, as in this range of scales the power  $S^D$  represents no more than some regridding noise and aliasing in the DCT.

The variance-excess coefficient  $\eta_{qk}$  computed for the geopotential height is shown in percent in Fig. 11a, as a function of length scale and height. The sharp spectral gradient of  $\eta_{qk}$  at approximately 1000 km indicates the effective resolution of the driving NCEP–NCAR geopotential height. It can be seen that the amplitudes of the large-scale geopotential heights in the CRCM simulations are overestimated near the surface and underestimated at higher levels. The CRCM relative vorticity and divergence exhibit similar variance excesses at the large-scale range (not shown).

The time evolution of the deviation of the CRCM

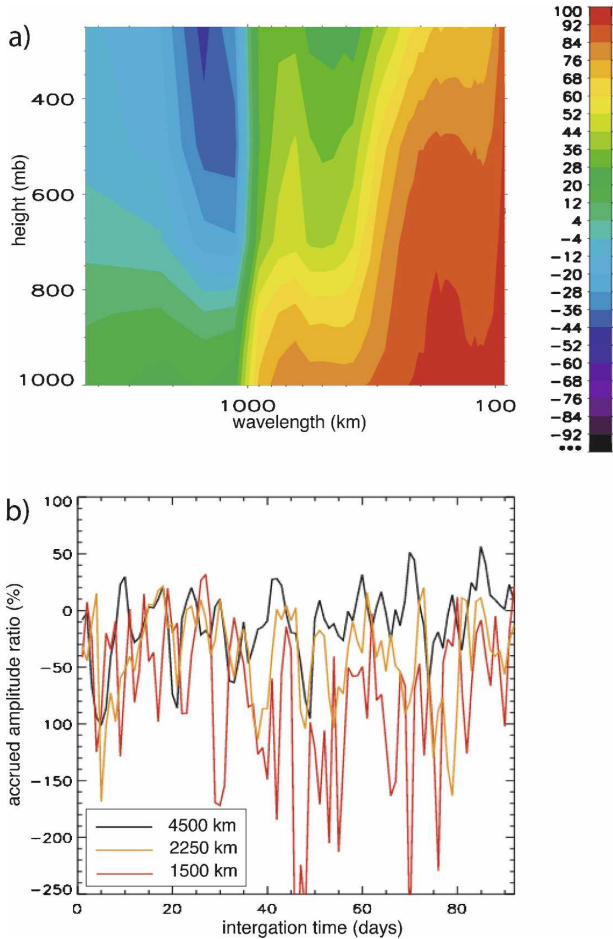


FIG. 11. (a) Representative variance-excess coefficient (%) of CRM geopotential height relative to the NCEP–NCAR reanalyses,  $\eta$  [defined in Eq. (11)], as a function of length scale and height. (b) The time evolution of the variance-excess coefficient [Eq. (12)] of the CRM geopotential height at 500 hPa as a function of time for the following length scales: black, 4500 km; yellow, 2250 km; and red, 1500 km.

power spectrum with respect to NCEP–NCAR is assessed by

$$\eta_{qkm} \equiv 1 - \frac{S_{qkm}^D}{S_{qkm}^A}. \quad (12)$$

Figure 11b shows the coefficient (12), in percent, for selected scales of the 500-hPa geopotential height as a function of time. The three largest length scales resolved by the CRM grid are shown: 4500, 2250, and 1500 km. At scales of 4500 km, the CRM generates a correct amount of variance despite the fact that large intermittent fluctuations of  $\eta_{qkm}$  are present. The earlier noted negative bias appears at scales of 2250 and 1500 km as being rather permanent. Furthermore, strong underestimations occur intermittently, with  $\eta_{qkm}$

as low as  $-250\%$ , indicating that average members' variance  $S^A$  is then 3.5 times smaller than the NCEP–NCAR-analyzed variance  $S^D$ . However, near the surface, although the CRM geopotential height large-scale variance is intermittently strongly underestimated, the average bias is positive.

It is worth mentioning that the variance-excess coefficient and the reproducibility ratio are not related. Figure 4 provides an illustrative example of the very weak spread among the members of the ensemble despite the fact that the members deviate considerably from the driving fields.

#### 4. Analysis of reproducible and irreproducible components of transient eddy variance

##### a. Definitions

The method employed in the previous section was based on the analysis of the reproducibility of the spatial variability at a specific time. Here, we examine the ability of the members in an ensemble to provide valuable information on the temporal evolution of the simulated variables at a given grid point. This is done by the separation of the temporal variance in its reproducible and irreproducible components.

The transient-eddy variances of individual realizations of the  $X_{ijkmn}$  field are computed by

$$\sigma_{ijkn}^2 = \sigma^2(X'_{ijkmn}) \equiv \overline{X'_{ijkmn}{}^2}, \quad (13)$$

where

$$X'_{ijkmn} \equiv X_{ijkmn} - \bar{X}_{ijkn}. \quad (14)$$

Here, the overbar denotes the seasonal average,  $(i, j)$  the horizontal grid index,  $k$  the level index,  $m$  the sampling time, and  $n$  the member in the ensemble. The ensemble average of the transient-eddy variance is defined as

$$\sigma_{ijk}^{2A} \equiv \langle \sigma^2(X'_{ijkmn}) \rangle, \quad (15)$$

and it can be decomposed into its reproducible and irreproducible components as

$$\sigma_{ijk}^{2A} = \sigma_{ijk}^{2R} + \sigma_{ijk}^{2I}, \quad (16)$$

where

$$\sigma_{ijk}^{2R} \equiv \sigma^2(\langle X' \rangle_{ijkm}) \quad \text{and} \quad (17)$$

$$\sigma_{ijk}^{2I} \equiv \langle \sigma^2(X'_{ijkmn}^*) \rangle. \quad (18)$$

Here,  $\sigma^{2R}$  represents the transient-eddy variance of the ensemble mean (the reproducible component on the ensemble) and  $\sigma^{2I}$  is the ensemble-average transient-

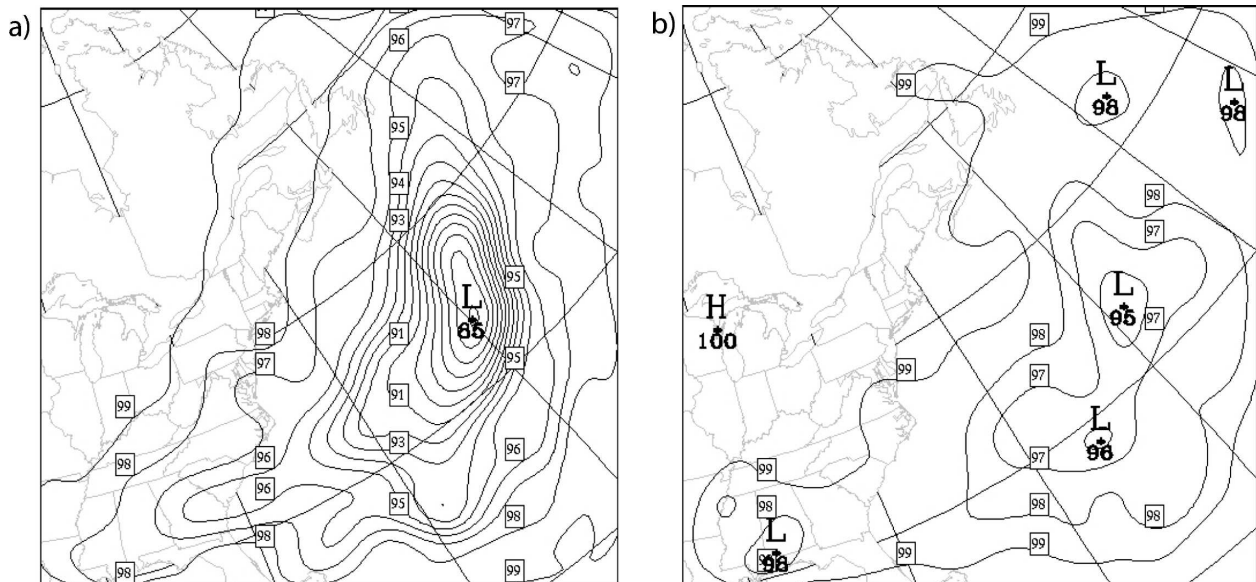


FIG. 12. Reproducibility ratio (%) of the transient-eddy variance of the large-scale components of the relative vorticity at (a) 925 and (b) 500 hPa.

eddy variance of the ensemble deviations (the irreproducible component).

Prior to computing the various transient-eddy variances, the CRCM-simulated fields are separated into their horizontal large-scale and small-scale components. The separation of scales is performed using the DCT filter described in Denis et al. (2002a). A low-pass (high pass) filter is used to preserve (remove) all scales larger than 1200 km and to remove (preserve) all scales smaller than 800 km; the resulting components of the simulated fields are denoted as the large-scale and the small-scale parts. The low-pass filter mimics the effective resolution of the driving fields, as was shown earlier, the effective resolution of the regridded NCEP–NCAR reanalyses is approximately 1000 km (e.g., Fig. 6).

The reproducibility ratio for transient eddies is defined as

$$\rho_{ijk} \equiv \frac{\sigma_{ijk}^{2R}}{\sigma_{ijk}^{2A}} \quad (19)$$

We examine the reproducibility ratios of large and small scales separately in the next two subsections. Without this separation of the scales, the internal variability at fine scales would be unnoticeable because of the high reproducibility of the large scales that contain the largest share of the variance. Note that in autonomous global models, beyond their predictability limit, Eq. (19) vanishes.

#### b. Reproducibility ratio of large-scale transient eddies

Figure 12 shows, in percentage, the reproducibility ratio of large-scale transient eddies of vorticity at 925 and 500 hPa. It approaches 100% at the perimeter of the domain, especially on the inflow, left side of the domain. It is lower over the ocean and the southeastern part of the continent especially over the Mississippi delta. This pattern of reproducibility is essentially preserved at all heights, although the lowest values are found near the ground (Fig. 12a). Other large-scale CRCM variables exhibit similar geographical distribution of their large-scale transient eddies' reproducibility ratio.

One possible reason to explain the minimum of reproducibility at the lowest level is the lower wind speed occurring near the surface. The control the LBC exert on the evolution of the RCM simulation by advection of information from the nesting zone toward the interior of the domain appears to increase with larger wind speed. Thus, the reproducibility of large scales at low levels may be smaller due to increased residence time of air parcels within the domain.

#### c. Reproducibility ratio of small-scale transient eddies

Inspection of the geographical distribution of the reproducibility ratio of the small-scale transient-eddy CRCM components shows patterns similar to those of

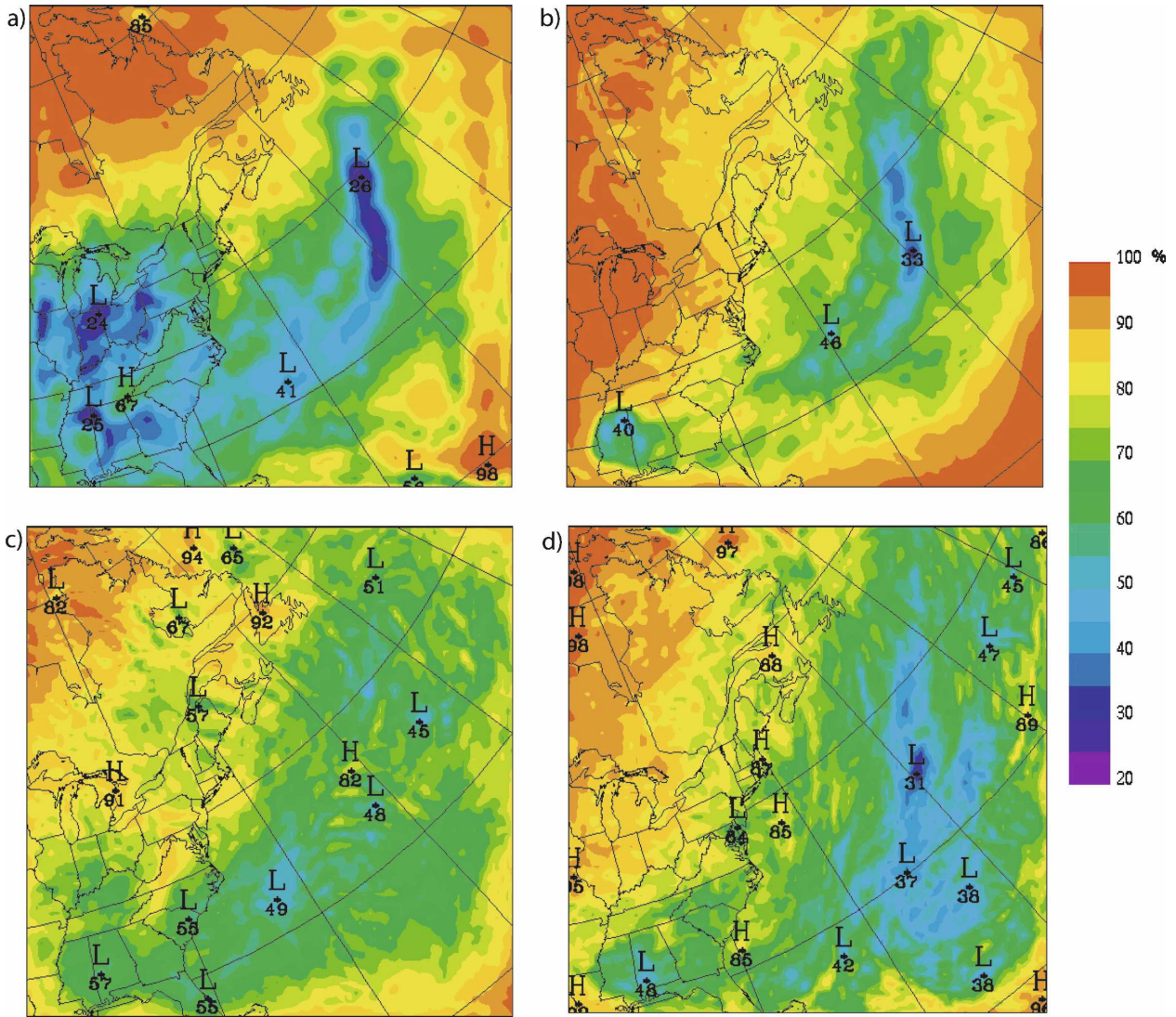


FIG. 13. Reproducibility ratio (%) of the transient-eddy variance of the small-scale components of the (a) geopotential height, (b) vorticity, (c) divergence, all at 700 hPa, and (d) 6-hourly precipitation.

the large scales, but with significantly smaller values. Although strongly influenced by the large scales, the small-scale components' reproducibility ratio appears to be more sensitive to variable, surface type, topography, and role that the convective processes and hydrodynamic instabilities play in the local climate than the reproducibility ratio of large scales.

Figure 13 shows the reproducibility ratio of transient-eddy small-scale CRCM variables at 700 hPa; it is at this level that the largest differences among the model variables occur. In the far northwestern part of the domain, the reproducibility ratio of the geopotential height (Fig. 13a) is very high, ranging from 90% to 100%, and decreases quickly toward the south, dropping to 20%–40% over a large part of the continent from the Gulf of

Mexico to the Great Lakes. The area of this minimum extends over the large part of the ocean. The long and narrow areas of very low reproducibility over the ocean are interpreted as trajectories of specific weather events giving rise to large ensemble spread. Such episodes are documented in Alexandru et al. (2007).

The geographical distribution of the reproducibility ratio of the transient-eddy variance of the small-scale vorticity (Fig. 13b) is quite different from that of the small-scale geopotential height. It is more tightly linked to the reproducibility ratio of the large-scale components (Fig. 12). This might be explained by the fact that the small-scale components of the vorticity are frequently embedded in synoptic low-pressure systems, where they appear as filaments associated with meso-

scale phenomena as fronts and thunderstorm lines. A slight temporal decorrelation between large-scale features simulated by two members of the ensemble will cause a strong temporal decorrelation of embedded small-scale features (de Elía et al. 2002), thus providing a strong dependence of the small-scale reproducibility ratio on that of larger scales.

The reproducibility ratio of the small-scale divergence is shown in Fig. 13c. The lowest values can be seen over the ocean but also over the continent, south of the Grate Lakes. The reproducibility ratio of the small-scale precipitation (Fig. 13d) is very similar to that of the low-level small-scale divergence.

It is worth mentioning that, unlike in the case for the large-scale components, the reproducibility ratio of the small-scale transient-eddy components is somewhat higher near the surface than aloft (not shown). This is in accordance with the vertical distribution of the reproducibility ratio of finescale CRCM spatial variances (Fig. 10).

### 5. Analysis of reproducible and irreproducible components of seasonal averages

We now turn our attention to seasonally averaged fields, which may also be called stationary-eddy components. These are again decomposed into their reproducible (ensemble mean) and irreproducible components, as well as being scale decomposed with the DCT. The ensemble-average stationary-eddy variance  $S^A$  and its reproducible ( $S^R$ ) and irreproducible ( $S^I$ ) components, are computed using Eqs. (5)–(7), for the seasonally averaged quantities rather than the instantaneous variables as was done in section 3.

Figure 14 shows the power spectra of these quantities for seasonal-average CRCM-simulated geopotential height, relative vorticity, divergence at 925 hPa, and precipitation, as well as the power spectra of the corresponding NCEP–NCAR reanalyses,  $S^D$ . For all seasonally averaged fields, the reproducible component (dashed line) dominates over the irreproducible component (dotted line) in the entire spectrum. However, the irreproducible component is less than an order of magnitude smaller than the reproducible at scales smaller than 200 km. For example, at these scales the reproducibility ratio of the seasonal precipitation (not shown) drops near 70%. It is also worth noting that, at finer length scales, the reproducibility ratio is found to be somewhat higher near the surface (not shown), revealing the weak constraint that the surface forcing imposes on the internal variability of the seasonal averages.

In the cases of vorticity (Fig. 14b) and divergence

(Fig. 14c), the ensemble average of the members' power spectra  $S^A$  (full line) is much larger than the power spectrum of the NCEP–NCAR fields (red line) at scales smaller than 1000 km, that is, beyond the effective resolution of the driving fields. This shows the ability of the CRCM to generate finescale details in seasonal climate statistics.

### 6. Concluding remarks

The purpose of this work was to identify the components of the fields simulated by nested LAMs that are controlled by the LBCs in a deterministic sense (referred to as reproducible components) and those that are, in this sense, free and thus nonreproducible. A 20-member ensemble of integrations of the CRCM, driven by NCEP–NCAR reanalyses, was conducted for a summer season over a midlatitude domain. Model-simulated variables and their seasonal averages were decomposed into a reproducible signal, defined as the ensemble mean, and an irreproducible component resulting from internal variability about the ensemble mean. The partition of the model solution between these two components as a function of length scale, geographical position within the domain, height, and weather episodes during the season was examined.

The results support an optimistic point of view regarding the capability of nested RCMs to provide fine-scale details. The spatial variance of the simulated variables at scales finer than those resolved by the driving fields is significant, especially for the noisy variables associated with such finescale features as fronts and convection lines. This also holds for finescale seasonal averages.

However, the results show that due to model internal variability a considerable part of the downscaled information is not a unique response of the model to the given set of lateral and surface boundary conditions. The internal variability was shown to be the most pronounced at the smallest scales, while the large-scale flow is more strongly controlled by the LBCs. But even the large-scale components were intermittently affected with significant spread among members in the ensemble.

The reproducibility ratios of the large- and small-scale components of the CRCM variables exhibit relatively well correlated spatial and temporal patterns. The exception is the low reproducibility of the finescale components of the mass field over the continent that might be associated with convection.

The results revealed that the reproducibility ratio of the large-scale transient eddies has its minimum at low levels, while the reproducibility of the small-scale com-

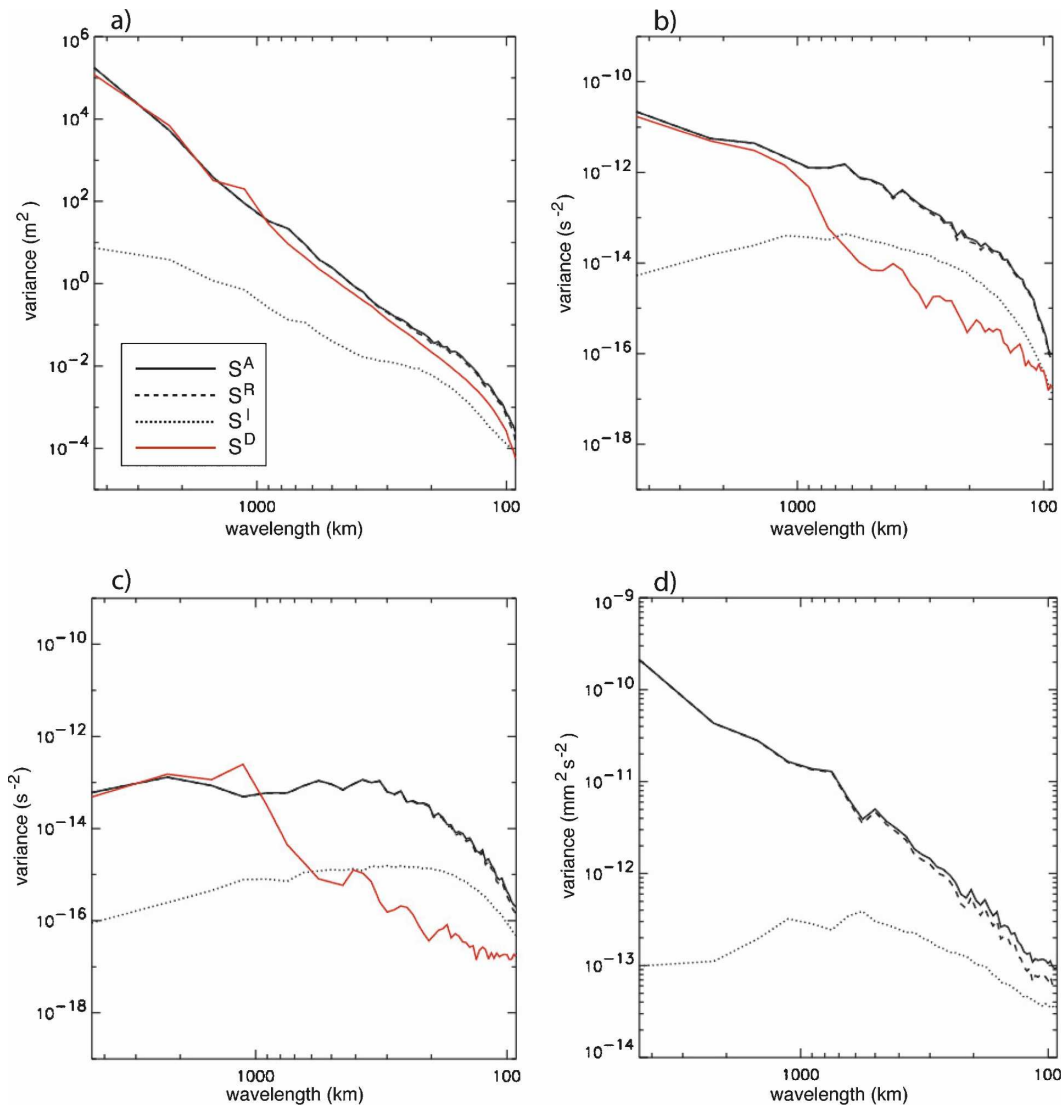


FIG. 14. Power spectra of seasonal-average CRCM (a) geopotential height, (b) vorticity, (c) divergence, all at 925 hPa, and (d) precipitation. Solid line represents the ensemble average of the members' power spectra, dashed line shows its reproducible part, and dotted line is its irreducible part. The red line is the spectral variance of the regridded NCEP-NCAR reanalyses (not available for precipitation).

ponents is somewhat higher for surface variables. Thus, the effect of surface forcing on the internal RCM variability might be twofold. Weaker flow speed and increased residence time at low levels might contribute to the reduction in the effective control of the LBCs at low levels; that is, the large-scale information provided at lateral boundaries is more likely to be forgotten at low levels. On the other hand, at finer scales topographic forcing and locally strong surface heterogeneities are likely to constrain the internal variability of the surface LAM small-scale variables.

The reproducible and irreducible components of the seasonal averages' power spectra are of comparable

magnitude at scales of a few hundreds of kilometers. These findings imply that for shorter RCM integrations the ensemble technique might be necessary, even if only lower moments of the climate statistics are of interest.

This study also revealed the fact that the amplitudes of the large-scale CRCM time-dependent variables are, on average, slightly overestimated near the surface and considerably underestimated in the upper troposphere, when compared to the variance of NCEP-NCAR driving fields. Castro et al. (2005) also reported a negative bias in the column-integrated kinetic energy large-scale spatial variance in their RCM simulations. This may

reflect an incapability of the model dynamics to support the correct amplitudes of the large-scale features at certain wavelengths (1500 km here). On the other hand, the lack of large-scale variance may represent an inherent problem in the “one-way nesting” concept of regional climate modeling. Large-scale nudging (e.g., Waldron et al. 1996; von Storch et al. 2000; Biner et al. 2000; Miguez-Macho et al. 2004; Castro et al. 2005) would prevent such differences. This issue calls for further investigation.

*Acknowledgments.* We thank the two anonymous reviewers for their valuable contributions to the final form of this manuscript. This research was done as a project within the Canadian Network for Regional Climate Modelling (CRCM) and the Canadian Network on Climate Variability (CLIVAR), funded by the Canadian Foundation for Climate and Atmospheric Sciences (CFCAS), the National Science and Engineering Research Council (NSERC), and the Ouranos Consortium on Regional Climatology and Adaptation to Climate Change.

## APPENDIX

### Reproducible and Irreproducible Components of Power Spectra

Let us assume that  $X_{jn}$  is the  $n$ th member of an ensemble of  $N$  realizations of a one-dimensional variable  $X$  defined in equidistant points  $j = 0, \dots, J - 1$ . The discrete Fourier transform of  $X_{jn}$  is given by

$$\Psi_{qn}(X) = \sum_{j=0}^{J-1} X_{jn} e^{-i \frac{2\pi qj}{J}}, \quad (\text{A1})$$

where  $i^2 = -1$ , and  $q \in \{0, 1, 2, \dots, J - 1\}$  represents the nondimensional wavenumber. The power spectrum of a variable  $X_{jn}$  is given by

$$S_{qn}(X) = \Psi_{qn}(X) \tilde{\Psi}_{qn}(X), \quad (\text{A2})$$

where the tilde ( $\sim$ ) denotes the complex conjugate.

On the other hand, the field  $X_{jn}$  can be decomposed as

$$X_{jn} = X_j^R + X_{jn}^I, \quad (\text{A3})$$

where

$$X_j^R = \langle X \rangle_j \equiv \frac{1}{N} \sum_{n=1}^N X_{jn} \quad (\text{A4})$$

is the reproducible part of the field  $X$ , that is, its ensemble average, and

$$X_{jn}^I \equiv X_{jn} - \langle X \rangle_j \quad (\text{A5})$$

is its irreproducible part, that is, the deviations from the ensemble mean. As the spectrum of  $X$  is linear in  $X$ , it can be decomposed as

$$\Psi_{qn}(X) = \Psi_q(X^R) + \Psi_{qn}(X^I). \quad (\text{A6})$$

Upon substituting (A6) in (A2), the power spectrum can be expressed as

$$S_{qn}(X) = S_q(X^R) + S_{qn}(X^I) + \tilde{\Psi}_q(X^R) \Psi_{qn}(X^I) + \Psi_q(X^R) \tilde{\Psi}_{qn}(X^I). \quad (\text{A7})$$

Applying the ensemble-average operator (A4) to Eq. (A7), the last two terms on the right-hand side vanish, and we obtain

$$\langle S_{qn}(X) \rangle = S_q(X^R) + \langle S_{qn}(X^I) \rangle, \quad (\text{A8})$$

which shows that the ensemble average of the individual members' power spectra can be decomposed into (i) the power spectrum of the reproducible part and (ii) the ensemble-average power spectrum of the irreproducible part of the field  $X$ .

## REFERENCES

- Alexandru, A., R. de Elia, and R. Laprise, 2007: Internal variability in regional climate downscaling at the seasonal scale. *Mon. Wea. Rev.*, **135**, 3221–3238.
- Anthes, R. A., Y. H. Kuo, D. P. Baumhefner, R. M. Errico, and T. W. Bettge, 1985: Predictability of mesoscale atmospheric motions. *Advances in Geophysics*, Vol. 288, Academic Press, 159–202.
- Bechtold, P., E. Bazile, F. Guichard, P. Mascart, and E. Richard, 2001: A mass flux convection scheme for regional and global models. *Quart. J. Roy. Meteor. Soc.*, **127**, 869–886.
- Biner, S., D. Caya, R. Laprise, and L. Spacek, 2000: Nesting of RCMs by imposing large scales. *Research Activities in Atmospheric and Oceanic Modelling*, H. Ritchie, Ed., WMO/TD 987, Rep. 30, 7.3–7.4.
- Boer, G. J., 2003: Predictability as a function of scale. *Atmos.–Ocean*, **41**, 203–215.
- Castro, C. L., R. A. Pielke Sr., and G. Leoncini, 2005: Dynamical downscaling: An assessment of value added using a regional climate model. *J. Geophys. Res.*, **110**, D05108, doi:10.1029/2004JD004721.
- Caya, D., and R. Laprise, 1999: A semi-implicit semi-Lagrangian regional climate model: The Canadian RCM. *Mon. Wea. Rev.*, **127**, 341–362.
- , and S. Biner, 2004: Internal variability of RCM simulations over an annual cycle. *Climate Dyn.*, **22**, 33–46.
- Christensen, O. B., M. A. Gaertner, J. A. Prego, and J. Polcher, 2001: Internal variability of regional climate models. *Climate Dyn.*, **17**, 875–887.
- Davies, H. C., 1976: Lateral boundary formulation for multi-level prediction models. *Quart. J. Roy. Meteor. Soc.*, **102**, 405–418.
- , and R. E. Turner, 1977: Updating prediction models by dynamical relaxation: An examination of the technique. *Quart. J. Roy. Meteor. Soc.*, **103**, 225–245.
- de Elía, R., R. Laprise, and B. Denis, 2002: Forecasting skill limits

- of nested, limited-area models: A perfect model approach. *Mon. Wea. Rev.*, **130**, 2006–2023.
- Denis, B., J. Côté, and R. Laprise, 2002a: Spectral decomposition of two-dimensional atmospheric fields on limited-area domains using the discrete cosine transform (DCT). *Mon. Wea. Rev.*, **130**, 1812–1829.
- , R. Laprise, D. Caya, and J. Cote, 2002b: Downscaling ability of one-way nested regional climate models: The big-brother experiment. *Climate Dyn.*, **18**, 627–646.
- Gal-Chen, T., and R. C. J. Somerville, 1975: On the use of a coordinate transformation for the solution of the Navier–Stokes equations. *J. Comput. Phys.*, **17**, 209–228.
- Gates, W. L., 1992: AMIP: The Atmospheric Model Intercomparison Project. *Bull. Amer. Meteor. Soc.*, **73**, 1962–1970.
- Giorgi, F., and L. O. Mearns, 1999: Introduction to special section: Regional climate modelling revisited. *J. Geophys. Res.*, **104** (D6), 6335–6352.
- , and X. Bi, 2000: A study of internal variability of a regional climate model. *J. Geophys. Res.*, **105** (D24), 29 503–29 521.
- Jones, R. G., J. M. Murphy, M. Noguer, and M. Keen, 1997: Simulation of climate change over Europe using a nested regional-climate model. II: Comparison of driving and regional model responses to a doubling of carbon dioxide. *Quart. J. Roy. Meteor. Soc.*, **123**, 265–292.
- Kalnay, E., and Coauthors, 1996: The NCEP/NCAR 40-Year Reanalysis Project. *Bull. Amer. Meteor. Soc.*, **77**, 437–471.
- Laprise, R., D. Caya, D. Bergeron, and M. Giguère, 1997: The formulation of André Robert MC2 (Mesoscale Compressible Community) model. *The André J. Robert Memorial Volume*, C. Lin, R. Laprise, and H. Ritchie, Eds., NRC Research Press, 195–220.
- , M. R. Varma, B. Denis, D. Caya, and I. Zawadzki, 2000: Predictability of a nested limited-area model. *Mon. Wea. Rev.*, **128**, 4149–4154.
- , and Coauthors, 2008: Challenging some tenets of regional climate modelling. *Meteor. Atmos. Phys.*, **100**, 3–22.
- Lorenz, E. N., 1969: The predictability of a flow which possesses many scales of motion. *Tellus*, **21**, 289–307.
- , 1982: Atmospheric predictability experiments with a large numerical model. *Tellus*, **34**, 505–513.
- Míguez-Macho, G., G. L. Stenchikov, and A. Robock, 2004: Spectral nudging to eliminate the effects of domain position and geometry in regional climate simulations. *J. Geophys. Res.*, **109**, D13104, doi:10.1029/2003JD004495.
- Rinke, A., P. Marbaix, and K. Dethloff, 2004: Internal variability in Arctic regional climate simulations: Case study for the SHEBA year. *Climate Res.*, **27**, 197–209.
- Robert, A., and E. Yakimiw, 1986: Identification and elimination of an inflow boundary computational solution in limited area model integrations. *Atmos.–Ocean*, **24**, 369–385.
- Schubert, D., and M. Suarez, 1989: Dynamical predictability in a simple general circulation model: Average error growth. *J. Atmos. Sci.*, **46**, 353–370.
- Tan, Z. M., F. Zhang, R. Rotunno, and C. Snyder, 2004: Mesoscale predictability of moist baroclinic waves: Experiments with parameterized convection. *J. Atmos. Sci.*, **61**, 1794–1804.
- van Tuyl, A. H., and R. M. Errico, 1989: Scale interaction and predictability in mesoscale model. *Mon. Wea. Rev.*, **117**, 495–517.
- von Storch, H., H. Langenberg, and F. Feser, 2000: A spectral nudging technique for dynamical downscaling purposes. *Mon. Wea. Rev.*, **128**, 3664–3673.
- Vukicevic, T., and J. Paegle, 1989: The influences of one-way interacting lateral boundary conditions upon predictability of flow in bounded numerical models. *Mon. Wea. Rev.*, **117**, 340–350.
- , and R. M. Errico, 1990: The influence of artificial and physical factors upon predictability estimates using a complex limited-area model. *Mon. Wea. Rev.*, **118**, 1460–1482.
- Waldron, K. M., J. Paegle, and J. D. Horel, 1996: Sensitivity of a spectrally filtered and nudged limited-area model to outer model options. *Mon. Wea. Rev.*, **124**, 529–547.
- Weisse, R., H. Heyen, and H. von Storch, 2000: Sensitivity of a regional atmospheric model to a sea state-dependent roughness and the need for ensemble calculations. *Mon. Wea. Rev.*, **128**, 3631–3643.
- Yakimiw, E., and A. Robert, 1990: Validation experiments for a nested grid-point regional forecast model. *Atmos.–Ocean*, **28**, 466–472.
- Zhang, F., C. Snyder, and R. Rotunno, 2003: Effects of moist convection on mesoscale predictability. *J. Atmos. Sci.*, **60**, 1173–1185.
- , N. Bei, R. Rotunno, and C. Snyder, 2007: Mesoscale predictability of moist baroclinic waves: Convection-permitting experiments and multistage error growth dynamics. *J. Atmos. Sci.*, **64**, 3579–3594.